Simultaneous control of crystallite size and interlayer spacing of MoS_2 to achieve pseudocapacitive lithium intercalation

Jaehoon Choi [a,b], Hyein Moon [a,b], Simon Fleischmann [a,b,*]

[a] *Helmholtz Institute Ulm (HIU), Helmholtzstr. 11, Ulm 89081, Federal Republic of Germany*
[b] *Karlsruhe Institute of Technology (KIT), Karlsruhe 76021, Federal Republic of Germany*

ARTICLE INFO

ABSTRACT

The functional properties of molybdenum disulfide (MoS_2) are highly dependent on its structure. Here, we present a one-pot hydrothermal synthesis approach allowing to simultaneous control MoS_2 structure over several length scales. Lowering the pH of the hydrothermal precursor solution leads to smaller crystallite sizes of the pristine MoS_2 formed. Moreover, the addition of alkyldiamines to the same precursor solution leads to their physical confinement between the forming MoS_2 layers without the formation of covalent bonds, yielding interlayer-expanded MoS_2. Controlling alkyldiamine precursor concentration can vary the number of confined structural pillars in interlayer-expanded MoS_2. Electrochemical lithium intercalation is tested as a function of MoS_2 structural properties. It is revealed that both smaller crystallite sizes and expanded interlayer-spacing lead to an increasingly pseudocapacitive lithium intercalation signature. The number of lithium that is reversibly stored in interlayer-expanded MoS_2 is increased to almost 1.5 per formula unit. The results provide a facile synthesis approach to simultaneously control MoS_2 crystallite size and d-spacing, which may be of interest for applications beyond lithium intercalation, such as multivalent ion intercalation or electrocatalytic hydrogen evolution.

1. Introduction

Transition metal dichalcogenides (TMDs, chemical formula MX_2, M = transition metal, X = S, Se, Te) are a class of two-dimensional materials consisting of individual MX_2 layers stacked by van der Waals forces. Among them, molybdenum disulfide (MoS_2) has been studied extensively in a wide range of fields such as electrochemical energy storage [1], electrocatalysis [2], electrochemical water desalination [3], or tribology [4]. As a consequence, a large number of synthesis approaches resulting in diverse morphologies and/or crystallite sizes are reported in literature [5].

While exfoliation or gas phase deposition methods like chemical vapor- or atomic layer deposition can produce mono-/few-layered materials with high precision [6], hydrothermal methods can be employed to obtain MoS_2 with varying morphologies in larger quantities. For the latter, morphology, particle/crystallite size, or crystallinity can be tuned by variation of synthesis parameters. Specifically, it was demonstrated that lowering the pH of the reactant solution of the hydrothermal synthesis will yield smaller crystallite sizes [7]. Other studies have shown that the lattice parameters of MoS_2 can be directly tuned, for example,

by the introduction of foreign species / pillars into the interlayer space, expanding the c-lattice parameter [8]. This includes top-down approaches like the topotactic insertion of alkylammonium cationic pillars as demonstrated by Schöllhorn et al., however a previous chemical reduction and ion exchange are required [9,10]. In summary, the structural properties of MoS_2 can be tuned individually by different approaches over several length scales, from macroscopic tuning of particle or crystallite size, down to the microscopic tuning of lattice parameters like the interlayer spacing [11]. It would be desirable to control MoS_2 structure over several length scales at once in a one-pot synthesis approach, allowing to readily tailor emerging MoS_2 functional properties.

Cook et al. demonstrated that the electrochemical ion intercalation properties in MoS_2 electrode materials are highly dependent on the MoS_2 crystallite size. The authors found that the phase transition during lithiation of bulk MoS_2 is suppressed in nanostructured MoS_2, leading to the emergence of solid-solution Li^+ intercalation with pseudocapacitive properties [12–14], that is, kinetics which are not limited by solid-state diffusion [15,16]. Yao et al. further demonstrate that, in addition to decreased crystallite sizes, also the introduction of lattice disorder can

enable such pseudocapacitive intercalation properties of MoS$_2$ [17].

Manipulating the interlayer distance, i.e., the geometry of the nanoconfined space between individual MoS$_2$ layers, has been described to promote electrochemical ion intercalation reactions by reducing diffusion barriers and increasing available ion storage sites [11]. The use of hydroxy pillars in a "3D porous graphene aerogel decorated with oxygen-incorporated MoS$_2$" led to an expanded MoS$_2$ interlayer spacing from 6.15 to 10.15 Å, resulting in increased Li$^+$ intercalation kinetics and storage capacity [18]. Similarly, hollow nanospheres of hydroxy-containing MoS$_2$ nanosheet subunits showed an interlayer spacing between 9.5 and 10.0 Å, also leading to improved kinetics and capacity of Li$^+$ intercalation [19].

Overall, the state-of-the-art literature on MoS$_2$ ion intercalation hosts clearly demonstrates that both, variation of particle/crystallite sizes and tuning of the interlayer spacing are viable strategies to improve ion intercalation kinetics and storage capacity. The former strategy improves kinetics by reducing diffusion distances and suppressing phase transformations, while the latter reduces diffusion barriers and increases storage sites. However, to date, no versatile synthesis approach to control both, crystallite size and interlayer spacing at once has been described. Furthermore, the understanding of MoS$_2$ host-pillar interaction in interlayer-expanded MoS$_2$ is insufficient and it is unclear how pillars behave during electrochemical cycling.

To address these points, this study presents a versatile, one-pot hydrothermal synthesis approach to simultaneously control MoS$_2$ crystallite size by pH adjustment, interlayer distance by the use of alkylamine organic pillars, and interlayer composition by varying pillar concentration. Organic pillars are interchangeable allowing to widely tune MoS$_2$ nanoconfinement chemistry *via* this approach [9,20,21]. Comprehensive structural investigation reveals the resulting morphology and crystallography as a function of synthesis parameters and clarifies the interaction between MoS$_2$ host and alkylamine pillars. Electrochemical lithium intercalation properties are conclusively linked to the MoS$_2$ structure, with pseudocapacitive intercalation properties being amplified for smaller crystallites, larger interlayer distances and reduced pillar concentration. While we demonstrate the viability of our materials for lithium intercalation, the findings may be of broader relevance. Crystallite size and/or interlayer engineering of TMDs are considered critical for, among others, intercalation of multivalent ions [22], metal ion adsorption for water purification [23,24], or electrocatalytic hydrogen evolution[25,26].

2. Experimental

2.1. Material synthesis

Molybdenum disulfide (MoS$_2$) samples were synthesized using a one-pot hydrothermal method, following the procedure outlined by Geng et al. [27]. 300 mg MoO$_3$ (Alfa Aesar), 450 mg thioacetamide (Thermo Fisher Scientific), and 3 g urea (Merck KGaA) were dissolved in 50 ml deionized water and stirred for 30 min in a glass beaker. To control the pH of the solution, 1 M hydrochloric acid (HCl, Merck) or 1 M lithium hydroxide (LiOH, Merck) were added as needed to reach either pH 1 (Nano-MoS$_2$) or pH 5.5 (Micro-MoS$_2$), respectively. The pH was measured using a pH meter (Blueline 14pH/Xylem Analytics). The solution was transferred to a 100 ml Teflon vessel, which was used for hydrothermal synthesis in an autoclave (BRHS-100, Berghof). The synthesis temperature was set at 235 °C and maintained for two hours after reaching the target temperature. The pressure in the autoclave was maintained at ca. 13–18 bar. The reaction products were collected by centrifugation at 6000 rpm for 10 min, followed by vacuum filtration with washing in deionized water and ethanol. The filtered powder was dried at 80 °C in an oven overnight.

Furthermore, interlayer-expanded MoS$_2$ samples were also synthesized by the one-pot hydrothermal approach. In this case, 1,6-hexanediamine (HDA), 1,8-octyldiamine (ODA) or 1,12-diaminododecane (DDDA) (all Thermo Fisher Scientific) were introduced to the precursor solution described in the previous section. The quantity of HDA/ODA/DDDA added was determined based on a molar ratio of 1:x between diamine and MoS$_2$, where x was either 1 or 0.5. Post addition of diamine, the pH of the hydrothermal solution was adjusted to pH 1. The synthesis conditions and methodology for the powder remained consistent with those employed for the pristine materials, with the exception of the synthesis temperature, which was set to 180 °C.

2.2. Material characterization

Powder X-ray diffraction (XRD) patterns of the MoS$_2$-based materials were obtained in Bragg-Brentano geometry using a Bruker D8 Advance diffractometer operating with a Cu Kα radiation source (λ = 1.5406 Å) using a 0.02° step size and a dwell time of 1 s. Powder size distribution analysis was performed using a laser diffraction particle size analyzer (Mastersizer 3000, Malvern) to measure the size of non-spherical particles by the dynamic light scattering (DLS) method. A mixture of isopropanol and deionized water (1:1 volumetric ratio) was used as a dispersant. Raman spectroscopy was performed on bulk powder samples using a Renishaw InVia confocal Raman microscope with a 532 nm excitation laser. The laser power was kept at 100 μW to prevent the decomposition of samples. At least three different spots were investigated to check the homogeneity of samples. Fourier transform infrared spectroscopy (FTIR) was carried out using the FTIR spectrometer Spectrum Two (PerkinElmer). Powders were measured at a resolution of 1 cm^{-1} with 20 scans in the range of 400–4000 cm^{-1}.

Thermogravimetry analysis was performed using a TG 209 F1 Libra thermal analyzer (Netzsch) under oxygen flow (20 ml/min) at a heating rate of 2 K/min. Scanning electron microscopy (SEM) imaging was performed on a field emission scanning electron microscope (Crossbeam x340, Zeiss) under 5 kV operation voltage. Transmission electron microscopy (TEM) measurements were performed using a Talos F200i (Thermo Fisher Scientific, formerly FEI) operating at an accelerating voltage of 80 kV. For TEM sample preparation, powders were ground using a pestle and mortar. Then, the carbon-coated Formvar film of a copper TEM grid was carefully rubbed on the fine powders. The surface chemistry of the MoS$_2$-based materials was analyzed in powder form by X-ray photoelectron spectroscopy (XPS). The powder XPS was conducted in a SPECS UHV system (FOCUS 500 equipped with monochromatic X-ray source, PHOIBOS 150 hemispherical energy analyzer with 2D DLD detector) using the Al Kα ($h\nu$ = 1486.6 eV) radiation. The spectra were collected at 200 W with a pass energy of 10 eV and a step-size of 0.1 eV in a fixed analyzer transmission mode. The collected spectra were later calibrated to the signal of C-C/C-H sp3 at 284.8 eV as a reference on CasaXPS software.

2.3. Electrode preparation and electrochemical characterization

The slurry consisted of 80 wt% active material (pristine MoS$_2$ or interlayer-expanded MoS$_2$), 10 wt% carbon black (CB), and 10 wt% polyvinylidene difluoride (PVDF). Pristine and interlayer-expanded MoS$_2$ powders were ground with CB using a pestle and mortar and transferred into a small container together with 2 wt% PVDF-containing N-Methyl-2-pyrrolidone (NMP) solution and then transferred into a speed mixer (ARE-250, Thinky), where it was mixed for 10 min at 1000 rpm. The wet mixture was coated on a carbon-coated aluminum foil with a wet film thickness of 60 μm using a doctor blade, and dried overnight in an oven at 80 °C to remove NMP solvent. Electrodes were punched using a handheld electrode cutter with a diameter of 12 mm. Electrodes were stored in an 80 °C oven overnight before being transferred into an argon-filled glovebox. Metallic lithium discs (Honjo, 14 mm diameter) were used as negative electrodes. 2032-type coin cells were assembled with a 1 mm thick stainless steel spacer, a stainless steel spring, and glass microfiber filter (Whatman grade GF/A) as a separator in a glovebox (MBraun, O$_2$, H$_2$O <0.1 ppm). 120 μl of LP30 electrolyte (1 M LiPF$_6$ in

ethylene carbonate (EC): dimethyl carbonate (DMC) (1:1 volumetric ratio), Solvionic) was used in each coin cell. Cyclic voltammetry (CV) and galvanostatic cycling tests were performed at different scan rates and currents between 1.0 and 3.0 V versus Li/Li^+ in temperature-controlled chambers (Binder) at 20 °C using a potentiostat (Bio-Logic VMP3-e and VMP300). Long-term cycling tests were conducted at 0.5 A/g.

For the *ex situ* XRD analysis, the same electrodes as prepared for the electrochemical characterization are utilized. 2032-type coin cells are assembled following the procedures detailed above. Using GCPL with a specific current of 0.05 A/g, the electrode is reduced to 1.0 V vs. Li^+/Li. The coin cell is subsequently disassembled in an Ar-filled glovebox. The electrode is gently rinsed with diethyl carbonate (DEC), and then transferred to the glovebox prechamber, where vacuum is applied for more than 10 min to ensure the complete removal of residual DEC from the electrode. After, the electrode is transferred back into the glovebox, fixed onto an airtight XRD holder with Kapton tape and sealed with a domed-shaped lid. Then, XRD patterns of the lithiated electrode are collected between 4 and 25° (2 theta) using a Bruker D8 Advance diffractometer operating with a Cu Kα radiation source ($\lambda = 1.5406$ Å) using a 0.02° step size and a dwell time of 3 s.

3. Results and discussion

A one-pot hydrothermal synthesis strategy for MoS_2 is developed that allows to simultaneously control both the crystallite size and geometric nanoconfinement environment (i.e., interlayer distance and guest species density) of the material. Pristine MoS_2 is obtained following a hydrothermal process outlined by Geng et al. [27], and the particle size is controlled by adjusting the pH of the precursor solution, with more acidic conditions yielding smaller particle sizes. The obtained MoS_2 materials then allow to study the influence of particle size on the electrochemical lithium intercalation properties. To analyze the impact of interlayer distance on lithium intercalation, MoS_2 materials with the same particle size, but varied interlayer distances are synthesized by facile adaptation of the one-pot route with added 1,6-hexanediamine (HDA) molecular pillars to the precursor solution (Fig. 1). Finally, variation of the HDA concentration allows to determine the influence of pillar population in the MoS_2 interlayer space (nanoconfinement chemistry) on lithium intercalation properties, while particle size and interlayer distance are kept constant. Particular emphasis is put on obtaining and characterizing model materials with well-defined structural properties, allowing to individually study the impact of a single structural parameter on the lithium intercalation process.

3.1. Influence of crystallite size

3.1.1. Structural characterization

Two MoS_2 samples are synthesized from precursor solutions with controlled pH value with the goal to achieve a variation in product crystallite size [7]. Small and large particle/crystallite sizes of the MoS_2 products are obtained from hydrothermal processes with aqueous precursor solutions of pH 1 and pH 5.5, and labelled nano-MoS_2 and micro-MoS_2, respectively.

SEM images of the products show the formation of larger secondary particles consisting of agglomerates of flake-shaped primary particles, with several microns of secondary particle size for nano-MoS_2 (Fig. 2A) and tens of microns for micro-MoS_2 (Fig. 2B). The differences in primary particle sizes are revealed at higher magnification, with nano-MoS_2 exhibiting lateral dimensions of the two-dimensional MoS_2 layers in the range of ca. 100 nm as well as a low thickness/number of layers well below 10 nm, as compared to micro-MoS_2 with lateral sizes around 500–1000 nm and a larger thickness (Fig. 2A and B, insets). The observations from SEM are confirmed by dynamic light scattering (DLS) analysis, which can quantify the size of MoS_2 secondary particle agglomerates, revealing that the average size of the nano-MoS_2
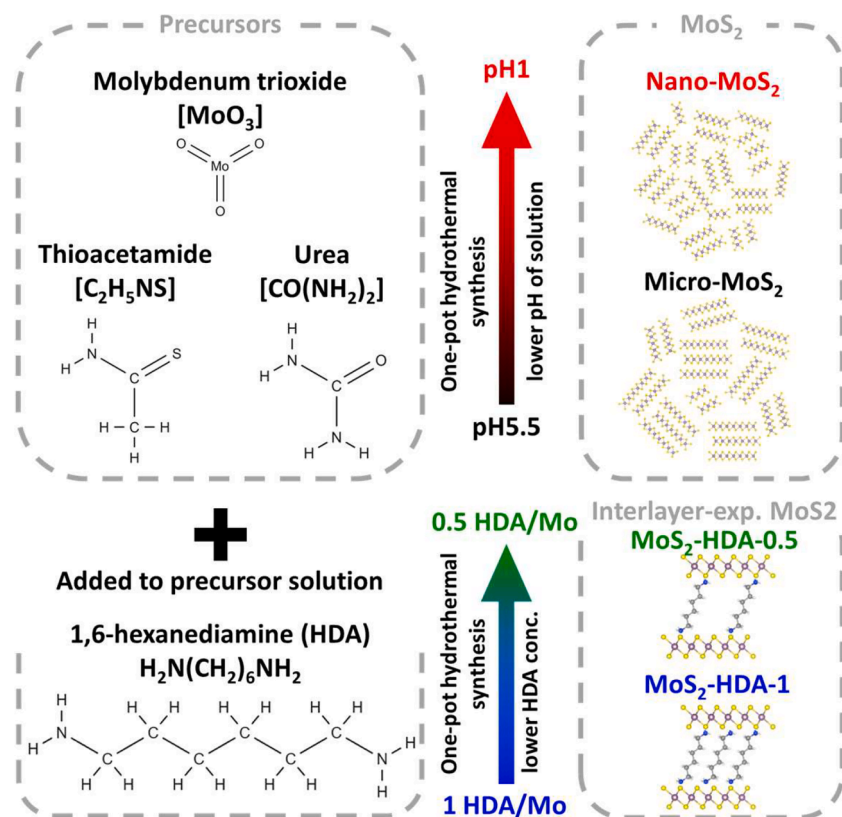
Fig. 1. Schematic illustration of the one-pot hydrothermal synthesis of MoS₂-based materials.
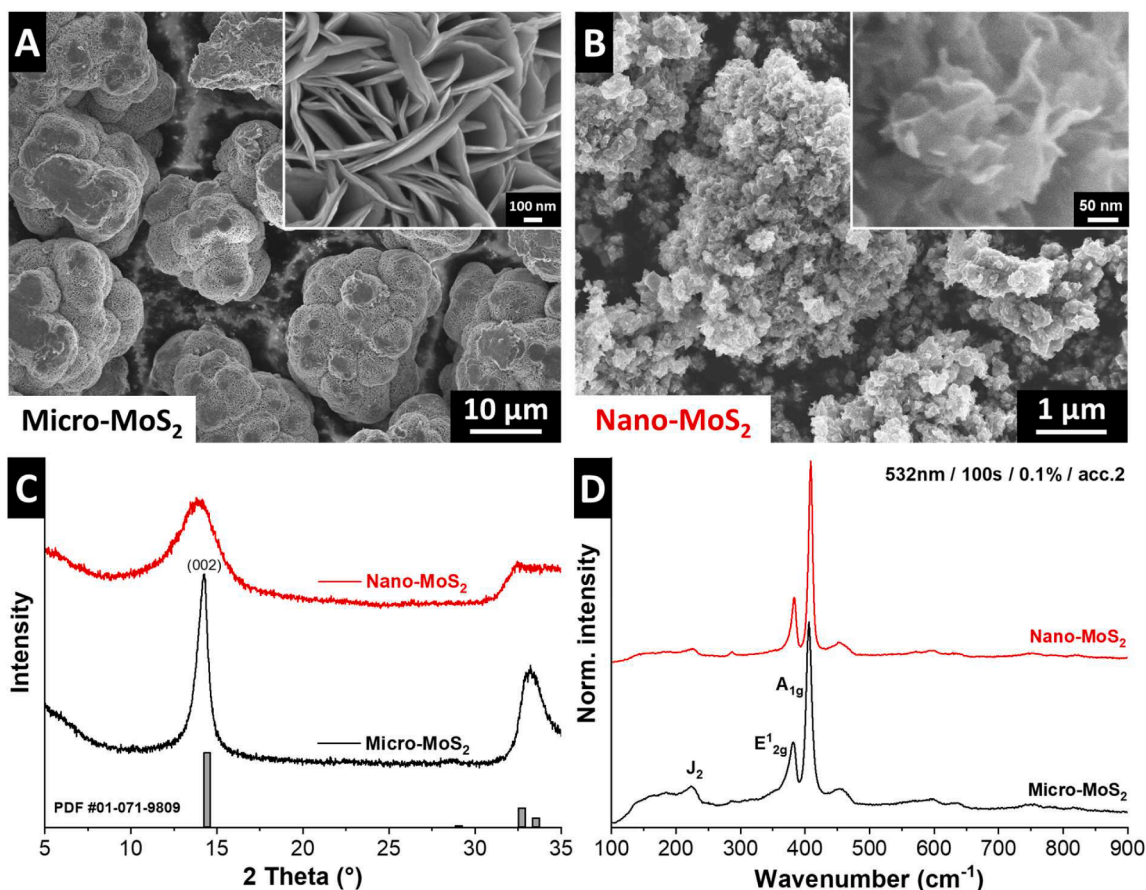
Fig. 2. SEM images of MoS$_2$ synthesized (A) at pH 5.5 yielding micro-MoS$_2$ and (B) at pH 1 yielding nano-MoS$_2$. (C) X-ray diffraction patterns including the ideal peak positions of hexagonal 2H-MoS$_2$ according to PDF card #01-071-9809 and (D) Raman spectra of both samples.

agglomerates is around 8 μm and that of micro-MoS$_2$ is around 26 μm (Fig. S1A).

X-ray diffraction (XRD) is utilized to assign the crystal structure of the synthesized materials as hexagonal 2H-MoS$_2$ according to PDF card #01-071-9809 (Fig. 2C). The interlayer distance is identified according to the (002) signal at ca. 13.9° 2θ as 6.15 Å for both nano-MoS$_2$ and micro-MoS$_2$ samples. A significant peak broadening of the (002) peak at 13.9° for nano-MoS$_2$ is a further qualitative confirmation of the reduced crystalline domain size compared to micro-MoS$_2$ [28]. Raman spectra of the two samples (Fig. 2D) show the two main characteristic peaks at 382 and 406 cm^{-1}, which correspond to E^1_{2g} and A_{1g} vibrational modes of the semi-conducting (2H) phase [29]. The results confirm that the employed hydrothermal synthesis route leads to the formation of 2H-MoS$_2$ [27], independent of crystallite size.

Overall, the structural investigation of nano-MoS$_2$ and micro-MoS$_2$ reveals that adjusting the pH of the precursor solution for the hydrothermal process to pH 1 or pH 5.5 is a suitable route to obtain 2H-MoS$_2$ materials with small or large crystallite sizes, respectively. The strategy thus allows to obtain model materials to study the influence of crystallite size on the lithium intercalation properties.

3.1.2. Electrochemical characterization

To understand the influence of the crystallite size of hydrothermally synthesized MoS$_2$ materials on electrochemical lithium intercalation behavior, the samples are investigated in a standard, lithium-containing organic electrolyte (1 M LiPF$_6$ in EC/DMC, LP30) using cyclic voltammetry (CV). The potential range is selected from 1.0 to 3.0 V vs. Li$^+$/Li, allowing to study the Li$^+$ intercalation reaction according to

$$MoS_2 + xLi^+ + xe^- \leftrightarrow Li_xMoS_2, \ 0 \leq x \leq 1, \tag{1}$$
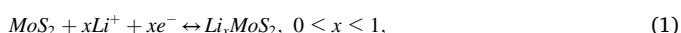
with a theoretical capacity of 167 mAh/g (for $x = 1$), without occurrence of the conversion-type reaction below 1.0 V vs. Li$^+$/Li [1]. The CV profiles of micro-MoS$_2$ and nano-MoS$_2$ are presented in Fig. 3A and B. At low sweep rates (up to ca. 1 mV/s), both samples reveal the presence of a redox signal centered around 1.7 V vs. Li$^+$/Li (cathodic sweep) and 1.9 V vs. Li$^+$/Li (anodic sweep) indicative of the Li$^+$ (de)intercalation reaction. For micro-MoS$_2$, it is visible that the signal is split into two separate peaks, while for nano-MoS$_2$, the signal is significantly broadened with the peaks apparently merging and a more significant rectangular current emerging. This behavior is indicative of an increasingly pseudocapacitive Li$^+$ intercalation behavior with decreasing crystallite size in nano-MoS$_2$, in line with previous reports [12,13,17]. Accordingly, at higher sweep rates above 10 mV/s, the CV signature of micro-MoS$_2$ rapidly becomes resistive, indicative of diffusion-limitations, while even at 100 mV/s a capacitor-like CV signal can be observed for nano-MoS$_2$ in line with kinetically favorable pseudocapacitive Li$^+$ intercalation [16].

Galvanostatic charge/discharge (GCD) tests are performed at constant specific currents between 0.02 and 5 A/g (Fig. 3C). At the lowest rate of 20 mA/g, both MoS$_2$ samples show a comparable first cycle anodic (delithiation) capacity of 175 and 182 mAh/g for micro-MoS$_2$ and nano-MoS$_2$, respectively, slightly above the theoretical capacity of 167 mAh/g for Li$_x$MoS$_2$ with $x = 1$. At higher rates, specifically above 1 A/g, nano-MoS$_2$ delivers significantly higher capacities due to the reduced kinetic limitations by solid-state diffusion, confirming the CV results. Nano-MoS$_2$ still exhibits a capacity of 90 mAh/g at a high rate of 5 A/g, which corresponds to a charge/discharge time of ca. 1 min, while micro-MoS$_2$ only exhibits 38 mAh/g. These values are quantitatively comparable to a study of Cook at el., probing lithium intercalation in bulk versus nanostructured MoS$_2$, where the latter was prepared by
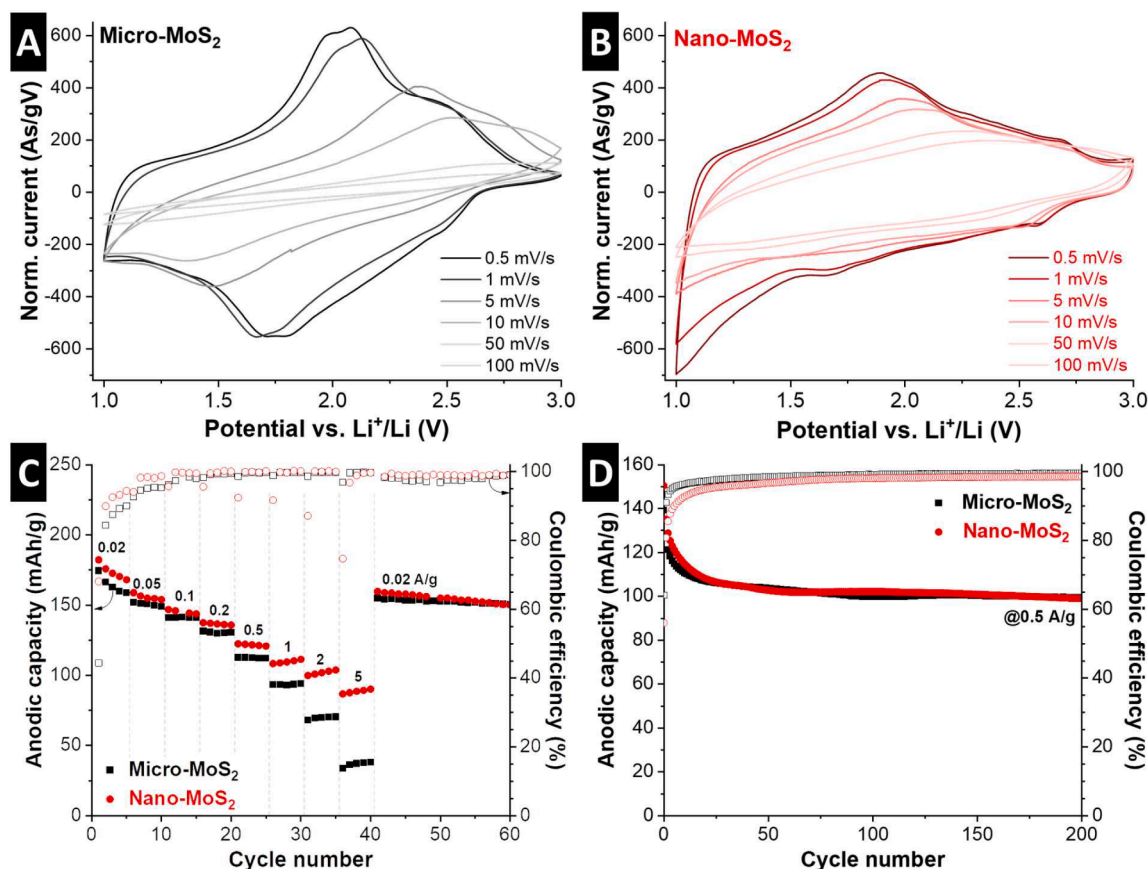
Fig. 3. Cyclic voltammograms of (A) micro-MoS$_2$ and (B) nano-MoS$_2$ at sweep rates from 0.5 to 100 mV/s. (C) Galvanostatic charge/discharge experiments at constant specific currents from 0.02 to 5 A/g and (D) galvanostatic cycling stability at a constant specific current of 0.5 A/g of both MoS$_2$ samples. All experiments carried out at 20 °C in coin cells against lithium metal in LP30 electrolyte.

thermal sulfurization of nanostructured MoO$_2$ in H$_2$S [12].

Galvanostatic cycling stability is tested at an intermediate rate of 0.5 A/g (Fig. 3D). A capacity drop in the initial 15 cycles can be observed, before both samples stabilize at around 105 mAh/g. This capacity remains relatively stable, reaching around 100 mAh/g after 200 cycles. We hypothesize that the initial capacity drop can be related to the ongoing phase transformation from semiconducting 2H to metallically conducting 1T phase of MoS$_2$ during initial lithiation cycles that has been described before [12]. To complete the phase transformation, it was reported that 4–8 cycles may be necessary depending on the MoS$_2$ crystallite size [12], which is reflected in the reduced Coulombic efficiency and capacity drop at low rates (Fig. 3C) as well as at higher rates (Fig. 3D) during the initial cycles. Hence a route to improve cycling stability could be utilizing fully 1T-transformed MoS$_2$.

It can be concluded that hydrothermally synthesized MoS$_2$ materials with facile crystallite size control *via* pH in this study show good agreement with the reported electrochemical performance of MoS$_2$ synthesized by other (more complex) approaches. In line with the initial goal of a multi-length scale control of MoS$_2$ structure, the next step is to further develop the best-performing nano-MoS$_2$ material on a microscopic, crystal structure level.

3.2. Influence of interlayer distance

3.2.1. Structural characterization

Building on the one-pot hydrothermal synthesis route outlined in the previous section, the precursor solution of nano-MoS$_2$ is adapted to additionally achieve microscopic control over the MoS$_2$ crystal structure to further improve the electrochemical performance. This is done *via* the addition of pillar molecules, namely 1,6-hexanediamine (HDA), which

we hypothesize will expand the interlayer space of MoS$_2$, modulating its geometric nanoconfinement environment. By using two different concentrations of HDA in the precursor solution (molar ratios of HDA/Mo of 1 and 0.5), the density of pillars is aimed to be controlled.

SEM characterization reveals comparable morphology with nano-MoS$_2$ samples, with few-micron sized secondary particles consisting of smaller flake-like primary particles with a lateral size in the range of 100 nm (Fig. 4A and B). Both MoS$_2$-HDA-1 and MoS$_2$-HDA-0.5 appear comparable to nano-MoS$_2$, indicating that the addition of HDA does not significantly affect the resulting MoS$_2$ morphology when the pH of the precursor solution remained at 1. Quantitative analysis *via* DLS confirms a comparable secondary particle size distribution with MoS$_2$-HDA-0.5 showing slightly reduced sizes (Fig. S1B).

XRD analysis shows the formation of MoS$_2$ with a shift of the (002) signal from 13.9° 2θ in nano-MoS$_2$ to 9.0° 2θ for both MoS$_2$-HDA-1 and MoS$_2$-HDA-0.5 samples (Fig. 4C). This confirms that the addition of HDA pillars to the precursor solution leads to the formation of interlayer-expanded MoS$_2$, with the (002) spacing expanding from 0.64 to 0.98 nm. The molecular conformation of HDA within the interlayer space has to be tilted with respect to the MoS$_2$ layers considering an estimated length of HDA including its van der Waals radius of around 1.22 nm. While the Raman spectrum of nano-MoS$_2$ revealed the formation of the semiconducting 2H phase, the spectra recorded for MoS$_2$-HDA-1 and MoS$_2$-HDA-0.5 samples show a distinctly different signature (Fig. 4D). The spectra show the characteristic vibrational Raman modes J$_1$ at 153 cm^{-1}, J$_2$ at 213 cm^{-1}, J$_3$ at 329 cm^{-1} and A$_{1g}$ at 412 cm^{-1} [29,30]. The spectra indicate the formation of a distorted 1T phase of MoS$_2$ (1T' phase) upon the confinement of HDA pillars as guest species in the MoS$_2$ interlayer space. The distorted 1T phase (1T') can be distinguished from the ideal 1T phase *via* the presence of the A$_{1g}$ mode at 412 cm^{-1} [31] and
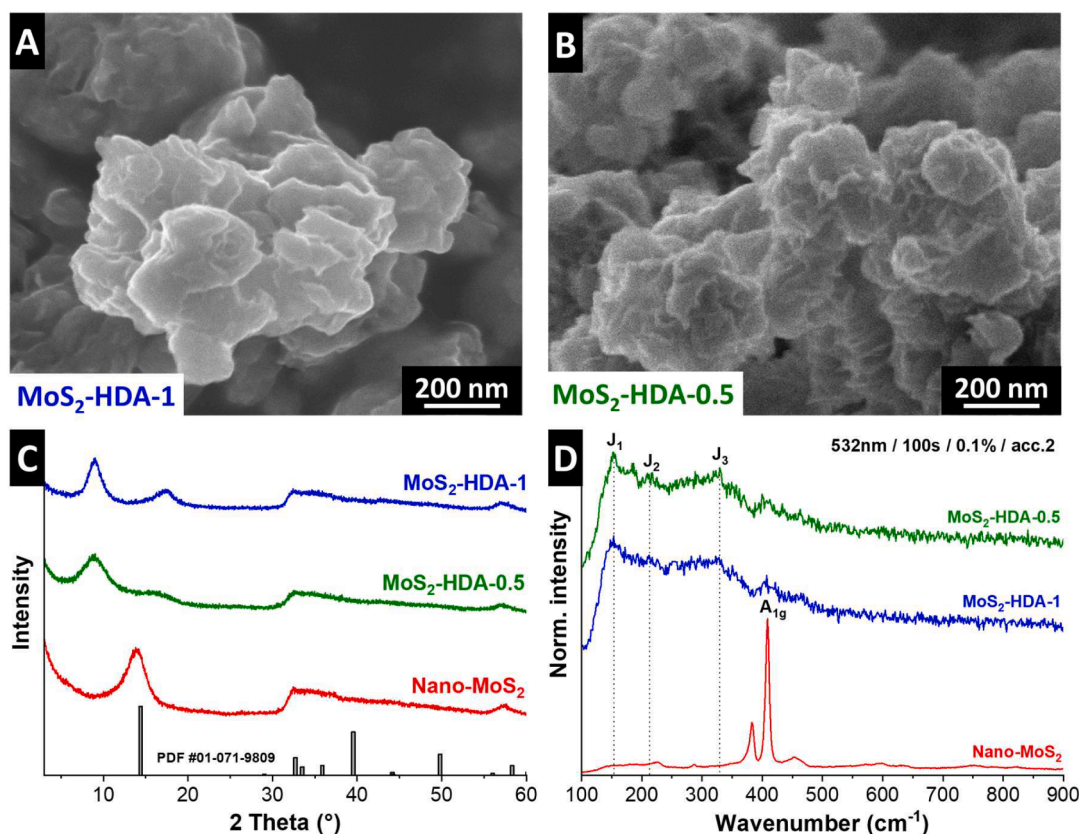
Fig. 4. SEM images of interlayer-expanded MoS$_2$ using 1,6-hexanediamine pillars with precursor molar ratios of HDA/Mo of (A) 1:1 and (B) 0.5:1. (C) XRD patterns and (D) Raman spectra of a nano-MoS$_2$ (same as in Fig. 2C and D, for comparison), MoS$_2$-HDA-1 and MoS$_2$-HDA-0.5 samples.

the absence of the E$_{2g}$ mode at 258 cm^{-1} [29]. We hypothesize that the 1T' phase forms as a consequence of the confined interlayer guest species (i.e., HDA pillars), which has been described for hydrothermally synthesized MoS$_2$ materials with various organic guest species before [32].

The HDA content of the samples is calculated from thermogravimetric analysis (TGA) under O$_2$-containing atmosphere that leads to a full burn-off of organic species (and concomitant MoS$_2$-to-MoO$_3$ transformation, Fig. S2). The calculated compositions for samples MoS$_2$-HDA-1 and MoS$_2$-HDA-0.5 are (HDA)$_{0.33}$MoS$_2$ and (HDA)$_{0.26}$MoS$_2$, respectively, confirming that the variation of HDA concentration in the precursor solution of the hydrothermal process can control the final composition of pillared MoS$_2$ to some extent. Furthermore, using Fourier transform infrared spectroscopy (FTIR), the presence of asymmetrical and symmetrical stretching vibrations of aliphatic C-H at 2915 and 2850 cm^{-1} [33], respectively, indicate that HDA does not decompose and remains intact under hydrothermal synthesis conditions (Fig. S3A). Additional verification is provided by the absence of D- and G-bands in their full Raman spectra, excluding the formation of amorphous carbon that would have resulted from HDA decomposition (Fig. S3B).

While the work mainly focusses on the interlayer-expansion of nano-MoS$_2$ because of its demonstrated superiority for electrochemical lithium intercalation, generalizability of the one-pot hydrothermal synthesis approach is further demonstrated. By adjusting pH to 5.5, interlayer-expansion of micro-MoS$_2$ with HDA is successfully performed (Fig. S4). Furthermore, interlayer-expansion of nano-MoS$_2$ at pH 1 is also feasible with 1,8-diaminooctane and 1,12-diaminododecane organic pillar molecules (Fig. S5).

Transmission electron microscopy (TEM) analysis of nano-MoS$_2$ and MoS$_2$-HDA-1 is carried out to obtain highly localized structural information of pristine versus interlayer-expanded MoS$_2$. The interlayer distances of both samples, as observed in the HRTEM images, closely

align with the values obtained from XRD patterns, with 0.63 nm for nano-MoS$_2$ (Fig. 5A) and 1.00 nm for MoS$_2$-HDA-1 (Fig. 5B). The values can be confirmed by the diameter of first ring of the selected area electron diffraction (SAED) patterns. Furthermore, the second and third rings in the SAED patterns, corresponding to the (100) and (110) planes, are at identical positions for nano-MoS$_2$ and MoS$_2$-HDA-1. This indicates the absence of in-plane structural changes in the individual MoS$_2$ sheets upon addition of HDA pillaring molecules in the interlayer space. It suggests that the interlayer expansion, facilitated by HDA, does not affect the host structure beyond geometric expansion. Our findings are in contrast to previous studies that reported significant structural and chemical in-plane modification of MoS$_2$, such as nitrogen-doping *via* sulfur-substitution after the addition of pillaring molecules during hydrothermal synthesis [26,32]. Furthermore, the distribution of HDA pillars is analyzed *via* energy-dispersive X-ray spectroscopy (EDX) in scanning transmission electron microscopy mode (STEM), confirming a homogenous distribution of nitrogen throughout the sample (Fig. S6). It should be noted that traces of nitrogen are also found in nano-MoS$_2$ (at much lower concentration, see Table S1), indicating small residues of thioacetamide and/or urea precursors.

The interaction of HDA molecules with the MoS$_2$ host lattice is investigated *via* X-ray photoelectron spectroscopy (XPS). The Mo 3d and S 2p spectra of the MoS$_2$-based materials are displayed in Fig. 6. To analyze the possibility of covalent bonding between HDA molecules and interlayer-expanded MoS$_2$ host, the spectra of MoS$_2$-HDA-1 (as the sample with the highest HDA-content) are directly compared with those of pristine, nano-MoS$_2$. In Fig. 6A, the most intense signals of characteristic Mo^{4+} at around 229.0 eV and 232.4 eV are attributed to MoS$_2$ [34]. Moreover, Mo^{4+} and Mo^{6+} from traces of precursor residue or/and oxidized MoS$_2$ at higher binding energies (i.e., MoO$_3$ and MoO$_2$) [35] are also present on the surface of the samples. However, the contributions are almost identical for both samples. The S 2p spectra in Fig. 6B
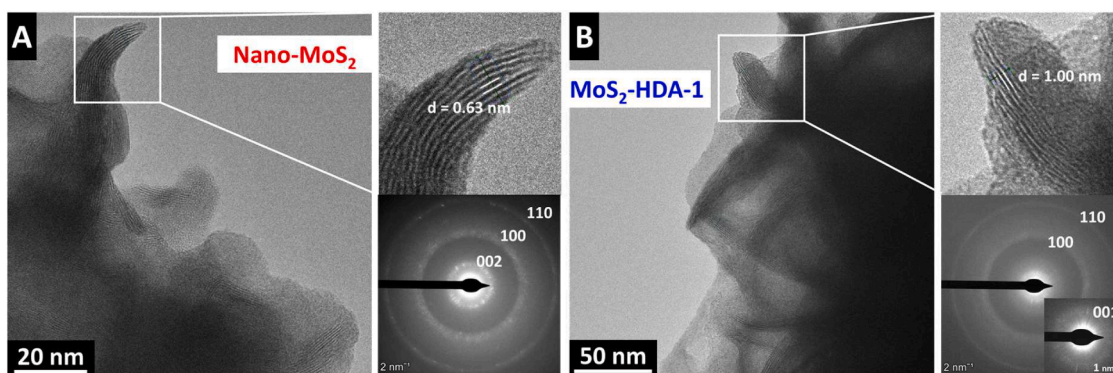
Fig. 5. HRTEM images and selected area electron diffraction patterns (obtained at 80 kV to avoid electron beam damaging) of (A) nano-MoS$_2$ and (B) interlayer-expanded MoS$_2$-HDA-1 samples.
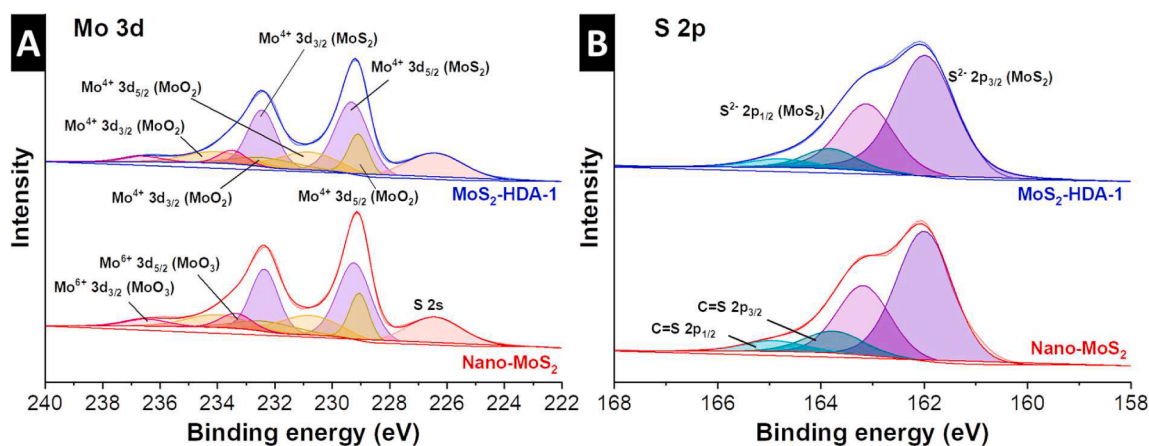
Fig. 6. X-ray photoelectron spectroscopy of (A) Mo 3d region and (B) S 2p region of nano-MoS$_2$ and MoS$_2$-HDA-1 samples.

include the MoS$_2$ related doublets at 162 eV and 163.1 eV, and the trace of organic sulfur (C=S) at 163.8 eV and 165 eV originating from the precursor (i.e., thioacetamide), suggesting precursor residues on the MoS$_2$ surface [36]. MoS$_2$-HDA-1 doublets in both regions show no apparent shifts in binding energy compared to the pristine nano-MoS$_2$ regardless of the interlayer-expansion found by XRD and TEM. Furthermore, the atomic concentration of each element acquired from survey data (Fig. S7 and Table S2) also presents highly comparable to each other. The absence of any additional contribution to the XPS signals in MoS$_2$-HDA-1 compared to nano-MoS$_2$ is indicative of a purely physical interaction as opposed to covalent bonding of the amine group to the MoS$_2$ host lattice [37]. The results are in support of the electron diffraction results from TEM analysis that suggest no alteration of in-plane MoS$_2$ structure in MoS$_2$-HDA-1 materials. Hence, the molecular pillaring approach *via* hydrothermal synthesis outlined in this work leads to MoS$_2$ with an expanded interlayer spacing with a purely physical host-pillar interaction in absence of in-plane structural changes. This is significant for the electrochemical analysis of the materials, because it allows for the electrochemical properties to be correlated with the expanded interlayer spacing, instead of being caused by a change of MoS$_2$ in-plane structure.

3.2.2. Electrochemical characterization

The structural characterization of HDA-pillared MoS$_2$ materials demonstrates that the materials exhibit an expanded interlayer spacing compared to nano-MoS$_2$, while other structural properties like morphology, crystallite size and in-plane MoS$_2$ structure remained similar. Furthermore, the concentration of HDA pillars is increased in MoS$_2$-HDA-1 compared to MoS$_2$-HDA-0.5. Consequently, the materials

can be used to study the influence of (1) interlayer spacing (i.e., nano-confinement geometry) and (2) pillar concentration (i.e., nanoconfine-ment chemical composition) on the electrochemical lithium intercalation performance.

The potential profiles of the first five galvanostatic cycles of nano-MoS$_2$, MoS$_2$-HDA-1 and MoS$_2$-HDA-0.5 at a constant specific current of 20 mA/g are shown in Fig. 7A–C. For nano-MoS$_2$, a low initial Coulombic efficiency (ICE, 44 %) is observed, which is correlated to the above described 2H-to-1T phase transformation in the plateau region around 1.1 V vs. Li$^+$/Li during the first lithiation (Fig. 7A) [38]. In comparison, both MoS$_2$-HDA-1 and MoS$_2$-HDA-0.5 exhibit higher ICEs of 65 % and 67 %, respectively, in absence of the 2H-to-1T phase transformation plateau. Instead, they likely undergo a 1T'-to-1T trans-formation during the first lithiation (vide infra) [31].

The initial anodic (delithiation) capacities of nano-MoS$_2$ and MoS$_2$-HDA-1 are in the same range (182 and 178 mAh/g, respectively), while the delithiation capacity of MoS$_2$-HDA-0.5 is increased to 199 mAh/g. Given that these values are normalized to the full composite mass of MoS$_2$ and HDA, the capacities of HDA-pillared materials significantly exceed that of nano-MoS$_2$ (1.09 Li$^+$) per transition metal, with 221 mAh/g$_{MoS2}$ or 1.32 Li$^+$ per MoS$_2$-HDA-1 and 237 mAh/g$_{MoS2}$ or 1.41 Li$^+$ per MoS$_2$-HDA-0.5. This is in line with previous reports of increased Li$^+$ storage in interlayer-expanded MoS$_2$ materials that potentially com-bines pseudocapacitive (Faradaic) Li$^+$ intercalation with an additional electric double-layer capacitance inside the widened interlayer galleries and/or at the solid/liquid interface [19,39].

Cyclic voltammograms of interlayer-expanded MoS$_2$ electrodes show an increased capacitor-like, rectangular current profile and the absence of the broad redox peak around 1.7–1.9 V vs. Li$^+$/Li as compared to
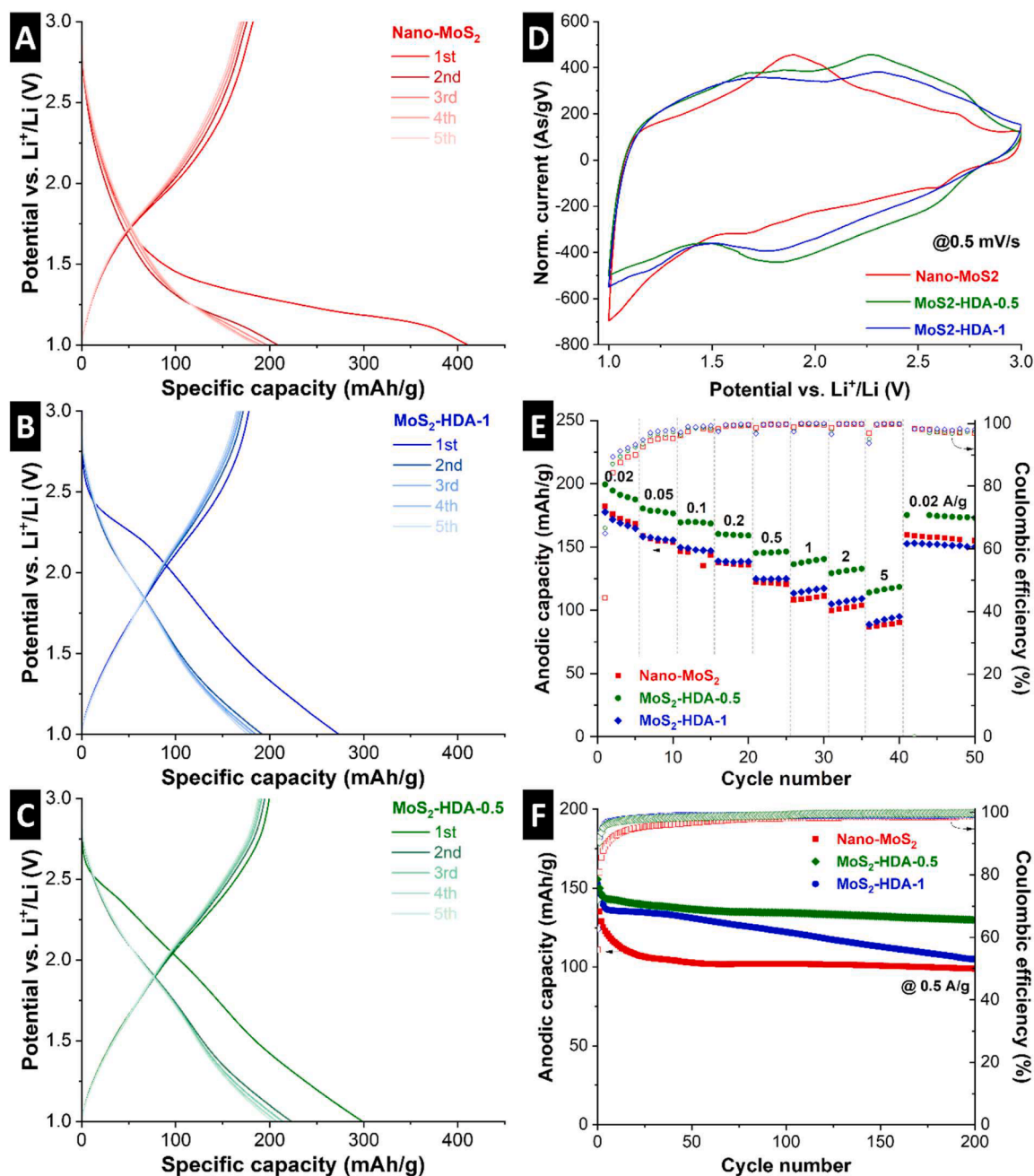
Fig. 7. Galvanostatic profiles of the first five cycles of (A) nano-MoS₂, (B) MoS₂-HDA-1 and (C) MoS₂-HDA-0.5 at a constant specific current of 20 mA/g. (D) Cyclic voltammograms of the three samples at a sweep rate of 0.5 mV/s. (E) GCD experiments at specific currents from 0.02 to 5 A/g and (F) galvanostatic cycling stability at a constant specific current of 0.5 A/g of the three samples. All experiments carried out at 20 °C in coin cells against lithium metal in LP30 electrolyte.

nano-MoS₂ (Fig. 7D). Given the lower content of electrochemically inactive HDA-pillars in MoS₂-HDA-0.5, its specific current signal has a slightly higher magnitude than MoS₂-HDA-1. The results indicate an increased pseudocapacitive Li⁺ intercalation behavior of interlayer-expanded MoS₂ compared to nano-MoS₂. The lithiation process of MoS₂-HDA-1 results in a further expansion from 0.98 to 1.06 nm as indicated by *ex situ* XRD (Fig. S8), whereas lithiation of pristine MoS₂ is known to not lead to significant changes in d-spacing (changes < 0.01 nm for fully lithiated MoS₂ of various crystallite sizes and degrees of disorder [17]). This is indicative of a larger number or size of inter-calating species into interlayer-expanded MoS₂, in line with the higher lithiation capacities measured for these samples (Li₁.₃₂-MoS₂-HDA-1 and Li₁.₄₁-MoS₂-HDA-0.5) compared to pristine MoS₂.

Quantitative GCD experiments (Fig. 7E) further underline the

superior Li⁺ intercalation performance of MoS₂-HDA-0.5 compared to the other samples. Its capacity retention of 118 mAh/g at a rate of 5 A/g corresponds to 63 % of the initial capacity (5th cycle at 20 mA/g) compared to 95 mAh/g for MoS₂-HDA-1 (58 %). The results underline that not only nanoconfinement geometry, i.e., an expanded interlayer spacing is beneficial for increased kinetics and storage capacity, but also the nanoconfinement chemical composition, i.e., the number of pillars determines electrochemical performance. The decreased number of pillars in MoS₂-HDA-0.5 not only reduces weight of (electrochemically) inactive component, but it is hypothesized that it is also beneficial for ion transport in the nanoconfined interlayer space [40].

The Li⁺ intercalation process is further analyzed *via* b-value analysis, where a b-value of 0.5 corresponds to diffusion-limited and a b-value of 1 to surface-limited intercalation kinetics (Fig. S9) [41]. While

decreasing of crystallite size shows an increase of the (cathodic) b-values from 0.85 for micro-MoS$_2$ to 0.93 for nano-MoS$_2$, the b-values for both MoS$_2$-HDA-0.5 and MoS$_2$-HDA-1 are also 0.93. Trends for the anodic b-values are similar. Overall, according to b-value analysis for sweep rates from 0.1 to 10 mV/s, there are no major differences in the kinetic limitations for all samples, with all of them exhibiting primarily surface-limited diffusion kinetics [16].

Galvanostatic cycling stability over 200 cycles at 0.5 A/g is shown in Fig. 7F. While nano-MoS$_2$ shows a significant initial capacity decay described in the previous Section 3.1.2, this initial decay is much smaller for both HDA-pillared samples. This can be explained by the absence of the 2H-to-1T transition for these samples, demonstrating the advantage of the 1T' phase formed for interlayer-expanded MoS$_2$. When comparing MoS$_2$-HDA-0.5 to MoS$_2$-HDA-1, the former shows significantly improved cycling stability. This is an indication that a reduced number of pillars confined in the interlayer space may be beneficial for cycling stability. The underlying mechanism and an investigation into the optimum number of pillars will be topic of future investigation using operando techniques and post-mortem cryogenic TEM analysis [42].

4. Conclusions

This study introduces a versatile one-pot hydrothermal synthesis strategy that enables simultaneous control of MoS$_2$ structure over several length scales, ranging from macroscopic crystallite size to microscopic lattice parameter control. Lowering the pH of the precursor solution for hydrothermal synthesis leads to the formation of smaller crystallites. The addition of alkyldiamines like 1,6-hexanediamine (HDA) to the same precursor solution will lead to their confinement between the forming MoS$_2$ layers, acting as structural pillars expanding MoS$_2$ interlayer spacing. By changing the HDA concentration, the content of structural pillars in interlayer-expanded MoS$_2$ can be varied to some extent. The interaction between HDA pillars and MoS$_2$ host is purely physical in absence of covalent bonding, with no significant crystallographic changes in the MoS$_2$ in-plane structure after pillaring.

The influence of each structural parameter on the electrochemical lithium intercalation properties can be systematically studied. It is found that smaller crystallite sizes, as well as expanded interlayer spacing, both lead to increasingly pseudocapacitive Li$^+$ intercalation properties with a more and more capacitor-like CV shape. Among interlayer-expanded MoS$_2$ materials, reducing the number of confined HDA structural pillars leads to an improved specific capacity, rate capability and cycling stability. The number of lithium reversibly intercalated in per MoS$_2$ ranges from ca. 1 in micro-MoS$_2$ to up to almost 1.5 in MoS$_2$-HDA-0.5, emphasizing the importance of nanoconfinement properties of MoS$_2$ for electrochemical ion intercalation. Future work should also explore the influence of changes in pillar chemistry, for example, to trifunctional pillars which may further stabilize the expanded MoS$_2$ structure.

The materials described can also be of interest to field of multivalent ion intercalation, where expanded interlayer distances can enable reduced electrostatic interaction between ion and host. Furthermore, the materials can be of interest as hydrogen evolution electrocatalysts, where both an expanded interlayer distance and reduced crystallite size can increase the number of electrochemically active sites.

CRediT authorship contribution statement

Jaehoon Choi: Conceptualization, Formal analysis, Investigation, Writing – original draft. **Hyein Moon:** Formal analysis, Investigation, Writing – review & editing. **Simon Fleischmann:** Conceptualization, Formal analysis, Funding acquisition, Project administration, Supervision, Writing – original draft, Writing – review & editing.

Declaration of competing interest

The authors declare that they have no known competing financial interests or personal relationships that could have appeared to influence the work reported in this paper.

Data availability

Data will be made available on request.

Supplementary materials

Supplementary material associated with this article can be found, in the online version, at doi:10.1016/j.electacta.2024.143774.

References

[1] T. Stephenson, Z. Li, B. Olsen, D. Mitlin, Lithium ion battery applications of molybdenum disulfide (MoS$_2$) nanocomposites, Energy Environ. Sci. 7 (2014) 209–231.

[2] Y. Cao, Roadmap and direction toward high-performance MoS$_2$ hydrogen evolution catalysts, ACS Nano 15 (2021) 11014–11039.

[3] P. Srimuk, J. Lee, S. Fleischmann, S. Choudhury, N. Jäckel, M. Zeiger, C. Kim, M. Aslan, V. Presser, Faradaic deionization of brackish and Sea Water via pseudocapacitive cation and anion intercalation into few-layered molybdenum disulfide, J. Mater. Chem. A 5 (2017) 15640–15649.

[4] A. Rosenkranz, Y. Liu, L. Yang, L. Chen, 2D nano-materials beyond graphene: from synthesis to tribological studies, Appl. Nanosci. 10 (2020) 3353–3388.

[5] X. Li, H. Zhu, Two-dimensional MoS$_2$: properties, preparation, and applications, J. Mater. 1 (2015) 33–44.

[6] N. Liu, P. Kim, J.H. Kim, J.H. Ye, S. Kim, C.J. Lee, Large-area atomically thin MoS$_2$ nanosheets prepared using electrochemical exfoliation, ACS Nano 8 (2014) 6902–6910.

[7] W. Hu, G. Han, F. Dai, Y. Liu, Effect of PH on the growth of MoS$_2$ (002) plane and electrocatalytic activity for HER, Int. J. Hydrogen Energy 41 (2015) 294–299.

[8] K.D. Rasamani, F. Alimohammadi, Y. Sun, Interlayer-expanded MoS$_2$, Mater. Today 20 (2017) 83–91.

[9] R. Schöllhorn, A. Weiss, R. Schbllhorn, A. Weiss, Cation exchange reactions and layer solvate complexes of ternary phases MxMoS$_2$, J. Less-Common Met. 36 (1974) 229–236.

[10] Y. Liang, H.D. Yoo, Y. Li, J. Shuai, H.A. Calderon, F.C. Robles Hernandez, L.C. Grabow, Y. Yao, F. Carlos, R. Hernandez, L.C. Grabow, Y. Yao, Interlayer-expanded molybdenum disulfide nanocomposites for electrochemical magnesium storage, Nano Lett. 15 (2015) 2194–2202.

[11] B. Chen, D. Chao, E. Liu, M. Jaroniec, N. Zhao, S.-Z. Qiao, Transition metal dichalcogenides for alkali metal ion batteries: engineering strategies at the atomic level, Energy Environ. Sci. 13 (2020) 1096–1131.

[12] J.B. Cook, T.C. Lin, H.-S. Kim, A. Siordia, B.S. Dunn, S.H. Tolbert, Suppression of electrochemically driven phase transitions in nanostructured MoS$_2$ pseudocapacitors probed using operando X-ray diffraction, ACS Nano 13 (2019) 1223–1231.

[13] J.B. Cook, H.S. Kim, Y. Yan, J.S. Ko, S. Robbennolt, B. Dunn, S.H. Tolbert, Mesoporous MoS$_2$ as a transition metal dichalcogenide exhibiting pseudocapacitive Li and Na-ion charge storage, Adv. Energy Mater. 6 (2016) 1501937.

[14] J.B. Cook, H.S. Kim, T.C. Lin, C.H. Lai, B. Dunn, S.H. Tolbert, Pseudocapacitive charge storage in thick composite MoS$_2$ nanocrystal-based electrodes, Adv. Energy Mater. 7 (2017) 1601283.

[15] C. Choi, D.S. Ashby, D.M. Butts, R.H. DeBlock, Q. Wei, J. Lau, B. Dunn, Achieving high energy density and high power density with pseudocapacitive materials, Nat. Rev. Mater. 5 (2020) 5–19.

[16] S. Fleischmann, J.B. Mitchell, R. Wang, C. Zhan, D.E. Jiang, V. Presser, V. Augustyn, Pseudocapacitance: from fundamental understanding to high power energy storage materials, Chem. Rev. 120 (2020) 6738–6782.

[17] Y. Yao, H. Cumberbatch, D.D. Robertson, M.A. Chin, R. Lamkin, S.H. Tolbert, On the interplay between size and disorder in suppressing intercalation-induced phase

transitions in pseudocapacitive nanostructured MoS₂, Adv. Funct. Mater. (2023) 2304896.

[18] S. Gong, G. Zhao, P. Lyu, K. Sun, A pseudolayered MoS₂ as Li-ion intercalation host with enhanced rate capability and durability, Small 14 (2018) 1803344.

[19] S. Gong, G. Zhao, P. Lyu, K. Sun, Insights into the intrinsic capacity of interlayer-expanded MoS₂ as a Li-ion intercalation host, J. Mater. Chem. A 7 (2019) 1187–1195.

[20] S. Fleischmann, M.A. Spencer, V. Augustyn, Electrochemical reactivity under confinement enabled by molecularly pillared 2D and layered materials, Chem. Mater. 32 (2020) 3325–3334.

[21] C. Zhou, D. Wang, F. Lagunas, B. Atterberry, M. Lei, H. Hu, Z. Zhou, A.S. Filatov, D. Jiang, A.J. Rossini, R.F. Klie, D.V. Talapin, Hybrid organic–inorganic two-dimensional metal carbide MXenes with amido- and imido-terminated surfaces, Nat. Chem. (2023), https://doi.org/10.1038/s41557-023-01288-w.

[22] X. Xue, R. Chen, C. Yan, P. Zhao, Y. Hu, W. Kong, H. Lin, L. Wang, Z. Jin, One-step synthesis of 2-ethylhexylamine pillared vanadium disulfide nanoflowers with ultralarge interlayer spacing for high-performance magnesium storage, Adv. Energy Mater. 9 (2019) 1900145.

[23] H. Sun, T. Wu, Y. Zhang, D.H.L. Ng, G. Wang, Structure-enhanced removal of Cr (VI) in aqueous solutions using MoS₂ ultrathin nanosheets, New J. Chem. 42 (2018) 9006–9015.

[24] Z. Li, R. Fan, Z. Hu, W. Li, H. Zhou, S. Kang, Y. Zhang, H. Zhang, G. Wang, Ethanol introduced synthesis of ultrastable 1T-MoS₂ for removal of Cr (VI), J. Hazard. Mater. 394 (2020) 122525.

[25] W. Hu, H. Liu, W. Dong, H. Akif Munir, X. Fan, X. Tian, L. Pang, Ammonium ions intercalated 1T/2H-MoS₂ with increased interlayer spacing for high-efficient electrocatalytic hydrogen evolution reaction, J. Electroanal. Chem. 949 (2023) 117882.

[26] I.H. Kwak, I.S. Kwon, H.G. Abbas, J. Seo, G. Jung, Y. Lee, D. Kim, J.P. Ahn, J. Park, H.S. Kang, Intercalated complexes of 1T′-MoS₂ nanosheets with alkylated phenylenediamines as excellent catalysts for electrochemical hydrogen evolution, J. Mater. Chem. A 7 (2019) 2334–2343.

[27] X. Geng, W. Sun, W. Wu, B. Chen, A. Al-Hilo, M. Benamara, H. Zhu, F. Watanabe, J. Cui, T.P. Chen, Pure and stable metallic phase molybdenum disulfide nanosheets for hydrogen evolution reaction, Nat. Commun. 7 (2016) 10672.

[28] N. Kumar, P. Siroha, H. Shankar, D. Singh, Y. Sharma, R. Kumar, R.N. Yadav, K. K. Dey, H. Borkar, J. Gangwar, K. KumarDey, H. Borkar, J. Gangwar, Probing into crystallography and morphology properties of MoS₂ nanoflowers synthesized *via* temperature dependent hydrothermal method, Nano Express 3 (2022) 035001.

[29] Y. Yu, G.H. Nam, Q. He, X.J. Wu, K. Zhang, Z. Yang, J. Chen, Q. Ma, M. Zhao, Z. Liu, F.R. Ran, X. Wang, H. Li, X. Huang, B. Li, Q. Xiong, Q. Zhang, Z. Liu, L. Gu, Y. Du, W. Huang, H. Zhang, High phase-purity 1T′-MoS₂- and 1T′-MoSe₂-layered crystals, Nat. Chem. 10 (2018) 638–643.

[30] G.-H. Nam, Q. He, X. Wang, Y. Yu, J. Chen, K. Zhang, Z. Yang, D. Hu, Z. Lai, B. Li, Q. Xiong, Q. Zhang, L. Gu, H. Zhang, In-plane anisotropic properties of 1T′-MoS₂ layers, Adv. Mater. 31 (2019) 1807764.

[31] X. Hou, W. Zhang, J. Peng, L. Zhou, J. Wu, K. Xie, Z. Fang, Phase transformation of 1T′-MoS₂ induced by electrochemical prelithiation for lithium-ion storage, ACS Appl. Energy Mater. 5 (2022) 11292–11303.

[32] I.H. Kwak, I.S. Kwon, H.G. Abbas, G. Jung, Y. Lee, T.T. Debela, S.J. Yoo, J.G. Kim, J. Park, H.S. Kang, Nitrogen-rich 1T′-MoS₂ layered nanostructures using alkyl amines for high catalytic performance toward hydrogen evolution, Nanoscale 10 (2018) 14726–14735.

[33] C.P. Marshall, E.J. Javaux, A.H. Knoll, M.R. Walter, Combined micro-Fourier transform infrared (FTIR) spectroscopy and micro-Raman spectroscopy of proterozoic acritarchs: a new approach to palaeobiology, Precambrian Res 138 (2005) 208–224.

[34] G.H. Major, N. Fairley, P.M.A. Sherwood, M.R. Linford, J. Terry, V. Fernandez, K. Artyushkova, Practical guide for curve fitting in X-ray photoelectron spectroscopy, J. Vac. Sci. Technol. A Vacuum Surf. Film. 38 (2020) 061203.

[35] D.O. Scanlon, G.W. Watson, D.J. Payne, G.R. Atkinson, R.G. Egdell, D.S.L. Law, Theoretical and experimental study of the electronic structures of MoO₃ and MoO₂, J. Phys. Chem. C 114 (2010) 4636–4645.

[36] J.D.P. Counsell, S.J. Coultas, N. Gerrard, MoS₂ by XPS using monochromatic Ag Lα x rays, Surf. Sci. Spectra 28 (2021) 024007.

[37] K.T. Park, J. Kong, Chemistry and physics of alkali metals on MoS₂ surfaces, Top. Catal. 18 (2002) 175–181.

[38] X. Fang, C. Hua, X. Guo, Y. Hu, Z. Wang, X. Gao, F. Wu, J. Wang, L. Chen, Lithium storage in commercial MoS₂ in different potential ranges, Electrochim. Acta 81 (2012) 155–160.

[39] S. Fleischmann, Y. Zhang, X. Wang, P.T. Cummings, J. Wu, P. Simon, Y. Gogotsi, V. Presser, V. Augustyn, Continuous transition from double-layer to Faradaic charge storage in confined electrolytes, Nat. Energy 7 (2022) 222–228.

[40] H. Banda, S. Périé, B. Daffos, P.L. Taberna, L. Dubois, O. Crosnier, P. Simon, D. Lee, G. De Paëpe, F. Duclairoir, Sparsely pillared graphene materials for high-performance supercapacitors: improving ion transport and storage capacity, ACS Nano 13 (2019) 1443–1453.

[41] J. Wang, J. Polleux, J. Lim, B. Dunn, Pseudocapacitive contributions to electrochemical energy storage in TiO₂ (anatase) nanoparticles, J. Phys. Chem. C 111 (2007) 14925–14931.

[42] Y. Shin, D. Stepien, M. Hepp, B. Butz, D. Bresser, S. Fleischmann, Cryogenic electron microscopy workflows for the characterization of electrochemical interfaces and interphases in batteries, J. Power Sources 556 (2023) 232515.